



1 **Counter-rotating eddy pair in the Luzon Strait**

2 Sun Ruili^{1,2*}, Li Peiliang^{1,3}, Gu Yanzhen³, Zhai Fangguo⁴, Yan Yunwei², Li Bo⁵

3 ¹Hainan Institute of Zhejiang University, Sanya, Hainan, China

4 ²State Key Laboratory of Satellite Ocean Environment Dynamics, Second Institute of

5 Oceanography, Ministry of Natural Resources, Hangzhou, China

6 ³Ocean college, Zhejiang University, Zhoushan, China

7 ⁴College of Oceanic and Atmospheric Sciences, Ocean University of China, Qingdao, China

8 ⁵State Key Laboratory of Tropical Oceanography, South China Sea Institute of Oceanology,

9 Chinese Academy of Sciences, Guangzhou, China

10 Corresponding author: Sun Ruili, sunruili2007@126.com

11 **Abstract:**

12 Based on satellite remote sensing observation data and Hybrid Coordinate Ocean Model
13 (HYCOM) reanalysis data, we studied the counter-rotating eddy pair in the Luzon Strait (LS).
14 Statistical analysis revealed that when an anticyclonic mesoscale eddy (AE) (cyclonic mesoscale
15 eddy (CE)) in the Northwest Pacific (NWP) gradually approached the east side of the LS, a CE (an
16 AE) gradually formed on the west side of the LS, and it was defined as the AE (CE) mode of the
17 counter-rotating eddy pair in the LS. The counter-rotating eddy pair exhibited obvious seasonal
18 variation: the AE mode mainly occurred in the summer half of the year, while the CE mode
19 mainly occurred in the winter half of the year. The mean durations of the AE mode and CE mode
20 were both about 70 days. Based on energy analysis and the vorticity budget equation, the dynamic
21 mechanism of the counter-rotating eddy pair occurrence was determined to be as follows: the AE
22 (CE) on the east side of the LS causes a positive (negative) vorticity anomaly through horizontal



23 velocity shear on the west side of the LS and the positive (negative) vorticity anomaly is
24 transported westward by the zonal advection of the vorticity, finally leading to the formation of the
25 CE (AE) on the west side of the LS.

26 **Keywords:** counter-rotating eddy pair; Luzon Strait; vorticity budget equation; barotropic
27 instability;

28 **1 Introduction**

29 The Luzon Strait (LS), located between the Taiwan Island and the Luzon Island, is an important
30 gap for material and energy exchange between the South China Sea (SCS) and the Northwest
31 Pacific (NWP). The topography around the LS is very complicated. The LS comprises three straits
32 from north to south: the Bashi Strait, the Balintang Strait and the Babuyan Strait. The Batanes
33 Islands and Babuyan Islands are located in these straights (Figure 1). These complex topographic
34 features can significantly affect the dynamic ocean process around the LS and play an important
35 role in the material and energy exchange between the SCS and the NWP (Lu and Liu, 2013; Sun et
36 al., 2016a). Sun et al (2016a) pointed out that the Kuroshio bifurcated into west and east branches
37 when it encounters the Batanes Islands in the LS. The bifurcation of the Kuroshio can significantly
38 alter the transport of the Kuroshio's main axis, and therefore, it has a potential impact on the
39 intrusion of the Kuroshio into the SCS. The bifurcation of the Kuroshio is also affected by
40 mesoscale eddies (Sun et al., 2016a).

41 Mesoscale eddies widely exist in the vicinity of the LS, and many of them come from the
42 NWP. These mesoscale eddies from the NWP can carry an enormous amount of kinetic energy and
43 can alter the local circulation, including the Kuroshio. Some of them cross the LS into the SCS,
44 thus contributing to the material and energy exchange between the SCS and the NWP. However, in



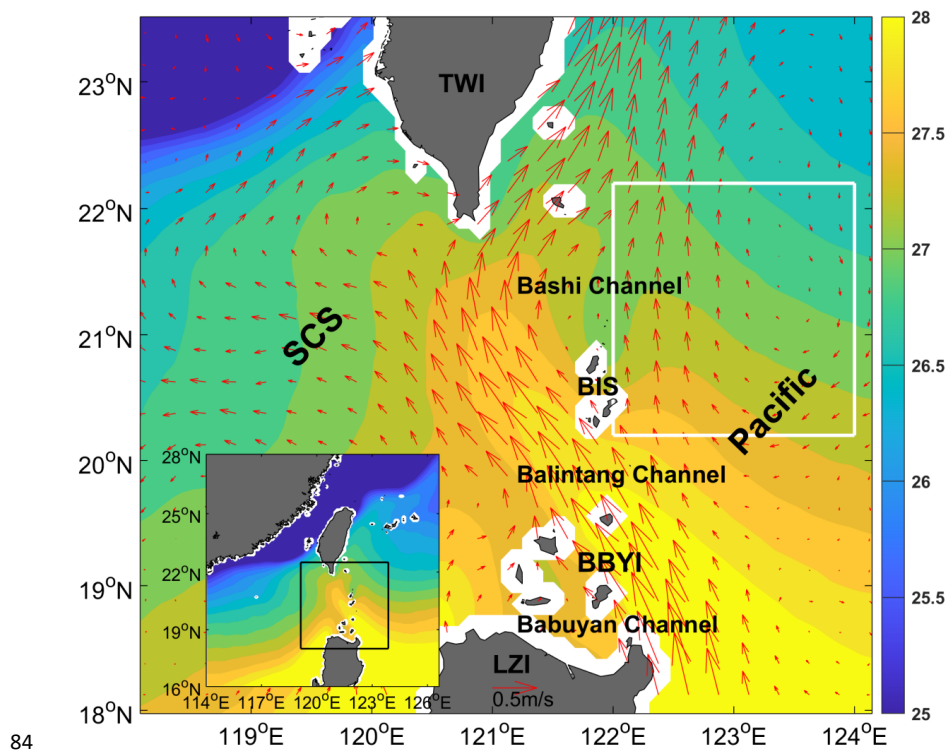
45 addition to their method of entering the SCS, it is important to determine if the mesoscale eddies
46 from the NWP affect the material and energy exchange between the SCS and WNP in other ways?
47 For example, mesoscale eddies from the NWP do not have to enter into the SCS, and they can
48 affect the SCS circulation through eddy-eddy interactions.

49 Numerous studies have been conducted on the eddy-eddy interactions in the vicinity of the
50 LS. Jing and Li (2003) used satellite remote sensing observation data to discover a cyclonic
51 mesoscale cold eddy around the Lanyu Island to the northeast of the LS, and they speculated that
52 the overshooting of the meandering Kuroshio when it leaves the SCS and the effects of the
53 conservation of the potential vorticity may be the formation mechanism of the Lanyu cold eddy.
54 Using a neural network and satellite remote sensing observation data, Yin et al. (2014) statistically
55 demonstrated that a CE (AE) from the NWP can decrease (increase) the velocity of the Kuroshio,
56 thus causing the Kuroshio to intrude into the East China Sea (ECS) in a stronger (weaker) cyclonic
57 manner. This showed that mesoscale eddies from the NWP can alter the ECS circulation without
58 entering the ECS. Sun et al (2016b) used updated satellite remote sensing observation data and
59 composition analysis to determine that the combined action of the Kuroshio loop and an AE from
60 the NWP led to the formation of the Lanyu cold eddy to the northeast of the LS. However, none of
61 these studies determined the dynamic mechanism of eddy-eddy interactions. Based on satellite
62 observation data, in situ observation data and numerical modelling data, Zhang et al. (2007)
63 analyzed the energy budget of the Kuroshio invading the SCS, and they determined that the
64 northern branch of the anticyclonic circulation caused by the Kuroshio loop has a large horizontal
65 shear stress and thus leads to the formation of a CE southwest of the Taiwan Island through the
66 barotropic instability, which proposed a dynamic mechanism for eddy-eddy interactions around



67 the LS.

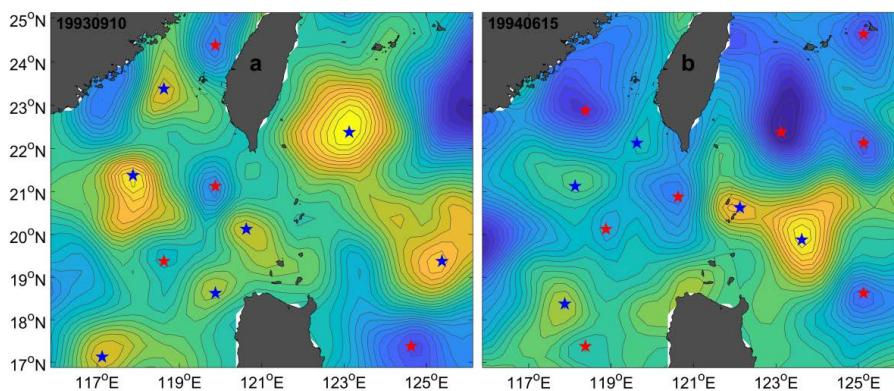
68 Although some research related to eddy-eddy interactions in the vicinity of the LS has been
69 conducted, and it has been discovered that mesoscale eddies are widely distributed on the west and
70 east sides of the LS (Figure 2), it is not clear whether the mesoscale eddies on the west and east
71 sides of the LS can interact and exchange energy between the SCS and the NWP. In order to
72 explore this issue, we compared the sea surface height anomaly (SSHA) distributions when a CE
73 occurred and when an AE occurred on the east side of the LS (Figure 3). The specific process will
74 be described in detail in Section 3.1. Figure 3 shows that when an AE (a CE) occurred on the east
75 side of the LS, a CE (an AE) formed on the west side of the LS, which was observed in the in situ
76 observation data (Huang et al., 2019). This is referred to as the counter-rotating eddy pair
77 phenomenon in this paper. This counter-rotating eddy pair process inevitably led to energy
78 exchange between the SCS and the NWP. To the best of our knowledge, it is not only a new
79 phenomenon proposed for the first time, but it is also a new mechanism proposed for the first time,
80 i.e., that energy is exchanged between the SCS and the NWP. We analyzed the statistical
81 characteristics and dynamic mechanism of this phenomenon. The rest of this paper is organized as
82 follows. Section 2 briefly introduces the data and methods. Section 3 presents the research results.
83 Section 4 presents the discussion and conclusion.



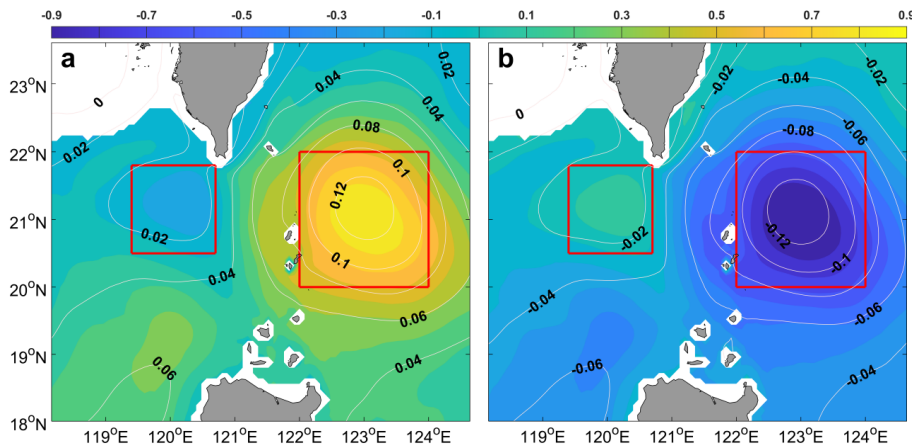
84

85 Figure 1. Spatial distribution of the RSS SST ($^{\circ}\text{C}$; shading) and CMEMS geostrophic current (m/s;
86 vectors) from 2003 to 2020. SCS: South China Sea; BIS: Batanes Islands; TWI: Taiwan Island;
87 LZI: Luzon Island; BBYI: Babuyan Islands. The white box borders 20.2-22.2 $^{\circ}\text{N}$, 122-124 $^{\circ}\text{E}$. The
88 extent of the main map is shown as a black box in the inset.

89



90
91 Figure 2. Spatial distribution of the CMEMS SSHA and locations of centers of the eddies on (a)
92 September 10, 1993 and (b) June 15, 1994. The colors and contours represent the SSHA. The blue
93 star and red star denote the locations of the AE and CE, respectively.



94
95 Figure 3. Spatial distribution of the counter-rotating eddy pair in the LS. (a) Spatial pattern of the
96 AE mode; and (b) Spatial pattern of the CE mode. The contours represent the SSHA (unit: m). The
97 colors represent the sea temperature anomaly (unit: °C) at a depth of 300 m. The interval of the
98 SSHA is 0.03 m. The red boxes on the west side and east side of the LS border 20.5-21.8°N,
99 119.4-120.7°E and 20-22°N, 122-124°E, respectively. This figure is similar to Figure 3 in Sun et
100 al (2018), and is based on HYCOM data.



101 **2 Data and methods**

102 2.1 Data

103 Satellite remote sensing SSHA, geostrophic current and geostrophic current anomaly data are
104 provided by the Copernicus Marine Environment Monitoring Service (CMEMS) (the download
105 website: [https://resources.marine.copernicus.eu/?option=com_csw&view=details&product_id=](https://resources.marine.copernicus.eu/?option=com_csw&view=details&product_id=SEALEVEL_GLO_PHY_L4_REP_OBSERVATIONS_008_047)
106 [SEALEVEL_GLO_PHY_L4_REP_OBSERVATIONS_008_047](https://resources.marine.copernicus.eu/?option=com_csw&view=details&product_id=SEALEVEL_GLO_PHY_L4_REP_OBSERVATIONS_008_047)). The data set is generated by
107 the processing system including data from all altimeter missions: Sentinel-3A/B, Jason-3, HY-2A,
108 Cryosat-2, OSTM/Jason-2, Jason-1, Topex/Poseidon, Envisat, GFO, ERS-1/2. The data set
109 provides a global coverage data from 1 January 1993 to present, with a spatial resolution of
110 $0.25^{\circ} \times 0.25^{\circ}$ and temporal sampling frequency of 1 day. It provides one near-real time component
111 and one delayed time component. The delayed time component has been inter-calibrated and
112 provided a homogeneous and highly accurate long time series of all altimeter data (Pujol and
113 Francoise, 2019), and is chosen in this paper.

114 Hybrid Coordinate Ocean Model (HYCOM) organization provided the HYCOM reanalysis
115 data (the download website: <https://www.hycom.org/dataserver/gofs-3pt0/reanalysis>). The data set
116 is based on ocean prediction system output, and the product with the longest time span from 2
117 October 1992 to 31 December 2012, is chosen among HYCOM data-assimilation product
118 provided by the HYCOM organization. The data set is based on ocean prediction system output
119 with a spatial resolution of $0.08^{\circ} \times 0.08^{\circ}$ and 40 standard z-levels between 80.48°S and 80.48°N . It
120 provides temperature, salinity, sea surface height, zonal flow and meridional flow.

121 The data set of wind was provided by the National Climate Data Center (NCDC) ([https://](https://www.ncdc.noaa.gov/data-access/marineocean-data/blended-global/blended-sea-winds)
122 www.ncdc.noaa.gov/data-access/marineocean-data/blended-global/blended-sea-winds). The data



123 set merges multiple satellite observation, in-situ instrument and related individual products. It
124 provides 6-hours, daily, monthly and climate data with a spatial resolution of $0.25^\circ \times 0.25^\circ$. The
125 data set contains globally gridded ocean surface vector winds and wind stresses (Zhang et al.,
126 2006).

127 Sea surface temperature (SST) data comes from Remote Sensing System (RSS; The download
128 websites: <http://www.remss.com/measurements/sea-surface-temperature/>). The data set merges
129 near-coastal capability and high spatial resolution of the infrared SST data with through-cloud
130 capabilities of the microwave SST data, and has applied atmospheric corrections. It provides daily
131 data with a spatial resolution of $9\text{km} \times 9\text{km}$ from July 1, 2002 to present.

132 2.2 Methods

133 2.2.1 Eddy energetic and hydrodynamic instability formula

134 The formation mechanisms of mesoscale eddies in the ocean are commonly attributed to
135 baroclinic and barotropic instabilities (Pedlosky, 1987; Zhang et al., 2015; Zhang et al., 2017). The
136 barotropic conversion (BT) and the baroclinic conversion (BC) are manifestations of the
137 baroclinic and barotropic instabilities, respectively, and they are the major eddy energy sources
138 around the LS (Yang et al., 2013; Zhang et al., 2013, 2015, 2017). In addition, the wind stress
139 work (WW) can also contribute to the formation of eddies (Ivchenko, 1997; Sun et al., 2015). The
140 BT, BC, and WW can be expressed as follows (Ivchenko, 1997; Oey, 2008):

$$141 \quad BT = - \int \left(\overline{u'^2} \frac{\partial \overline{u}}{\partial x} + \overline{v'^2} \frac{\partial \overline{v}}{\partial y} + \overline{u'v'} \frac{\partial \overline{u}}{\partial y} + \overline{u'v'} \frac{\partial \overline{v}}{\partial x} \right) dz, \quad (1)$$

$$142 \quad BC = - \int \frac{g^2}{\rho_0^2 N^2} \left(\overline{u'\rho'} \frac{\partial \overline{\rho}}{\partial x} + \overline{v'\rho'} \frac{\partial \overline{\rho}}{\partial y} \right) dz, \quad (2)$$

$$143 \quad WW = \frac{1}{\rho} \left(\overline{u'\tau'_x} + \overline{v'\tau'_y} \right), \quad (3)$$

144 Where t is the time; $u, v,$ and w are the zonal velocity, meridional velocity and vertical



145 velocity, respectively, and their positive directions are east, north and up, respectively. g is the
146 acceleration due to gravity; N is the buoyancy frequency; ρ is the density of sea water; $\rho_0 =$
147 $1030 \text{ kg} \cdot \text{m}^{-3}$ is the mean sea water density; p is the sea pressure; and τ_x and τ_y are the zonal
148 and meridional components of the wind stress, respectively. $x, y,$ and z are the conventional
149 east-west, north-south and up-down Cartesian coordinates, respectively. The depth integrals for
150 BT and BC are from 400m to the sea surface. The overbar denotes time averaged over an n -day
151 period, the primes denote deviations from the average, and the other symbols and notations are
152 standard. The n -day period was chosen to be 70 days according to the Figures 7 and 9, which
153 show that the period of the counter-rotating eddy pair phenomenon is close to 70 days. BT and BC
154 were calculated from the HYCOM data. CMEMS surface current velocity data and NCDC wind
155 data were used to calculate the WW.

156 2.2.2 Vorticity budget equation

157 To examine the influence of the vorticity change, we applied the vorticity budget equation:

$$158 \quad \frac{\partial \zeta}{\partial t} = -u \frac{\partial \zeta}{\partial x} - v \frac{\partial \zeta}{\partial y} - (\zeta + f) \nabla \cdot \vec{u} - v \frac{\partial f}{\partial y} + \frac{1}{\rho^2} \left(\frac{\partial \rho}{\partial x} \frac{\partial P}{\partial y} - \frac{\partial \rho}{\partial y} \frac{\partial P}{\partial x} \right) - v \frac{\partial^2 \zeta}{\partial z^2}, \quad (4)$$

159 Where $\zeta = \frac{\partial v}{\partial x} - \frac{\partial u}{\partial y}$ is the relative vorticity; t is the time; u and v is the zonal velocity,
160 meridional velocity, respectively. $x, y,$ and z are the conventional east-west, north-south and
161 up-down cartesian coordinates, respectively; f is the Coriolis parameter; ρ is the sea water
162 density; P is the sea water pressure; and ν is the kinematic viscosity coefficient. The items on the
163 right side of the equation are the zonal advection term, the meridional advection term, the
164 stretching term, the beta term, the baroclinic term and the diffusion term in turn.

165 3 Results

166 3.1 Identification of and temporal variation in the counter-rotating eddy pair in the LS

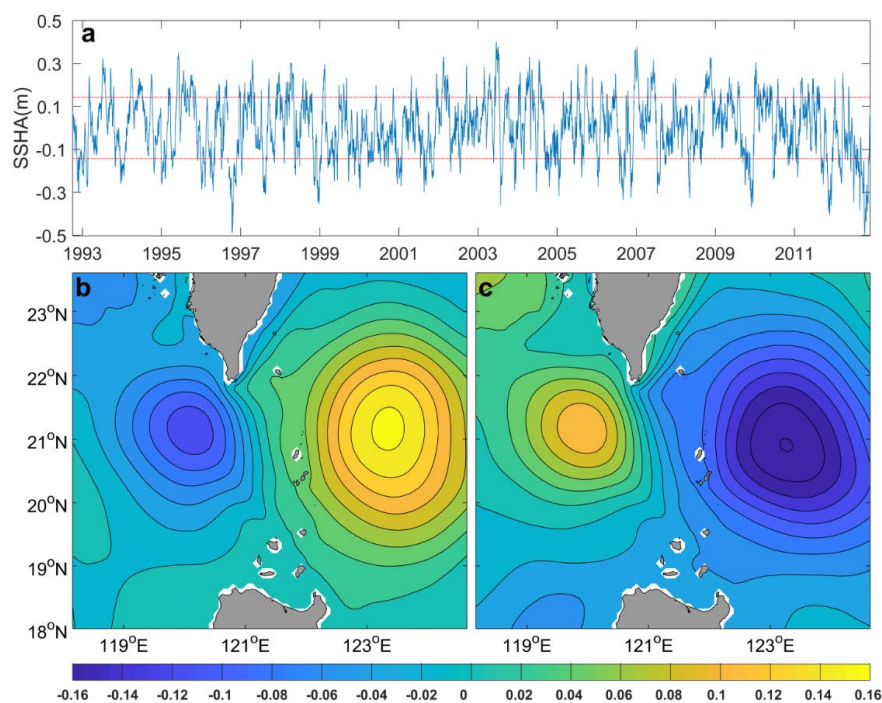


167 Based on cluster analysis, which is the same as the clustering method used by Sun et al. (2018),
168 we determined the SSHA and sea temperature anomaly (STA) based on the days when an AE and
169 a CE existed on the east side and west side of the LS (shown in the white box in Figure 1),
170 respectively. Figure 3 shows that when an AE (a CE) occurred on the east side of the LS, a CE (an
171 AE) formed on the west side of the LS, which is defined as a counter-rotating eddy pair in the LS
172 in this paper. Figure 3a shows that the SSHA in the red box on the east side of the LS increased
173 from the outside to the inside, which means that there was an AE. Due to the geostrophic balance
174 and mass conservation, the AE causes convergence of the sea water, leading to downwelling in its
175 center, subsequently leading to an increase in the temperature in the deep ocean. This is verified
176 by the fact that the STA in the red box on the east side of the LS is gradually increases from
177 outside to inside and the value is the highest in the center. In addition, the SSHA in the red box on
178 the west side of the LS decreases from outside to inside and the STA is negative, indicating the
179 presence of a weak CE. Figure 3b is similar to Figure 3a, but for a CE and an AE on the east and
180 west sides of the LS, respectively.

181 In order to better reflect the intensity of this phenomenon, we constructed an index which is
182 defined as the time series of the SSHA in the red box on the east side of the LS minus that on the
183 west side of the LS, in order to obtain a time series (Figure 4a). We constructed the SSHA based
184 on the days when the positive and negative intensity index values were more than one standard
185 deviation away from the mean. An AE (a CE) on the east side of the LS and a CE (an AE) on the
186 west side of the LS are shown in Figure 4b (Figure 4c) for the days with positive (negative)
187 intensity index values, which reflects the phenomenon of a counter-rotating eddy pair in the LS
188 well. The pattern in Figure 4b (Figure 4c) is defined as the AE (CE) mode of the counter-rotating



189 eddy pair in this paper.



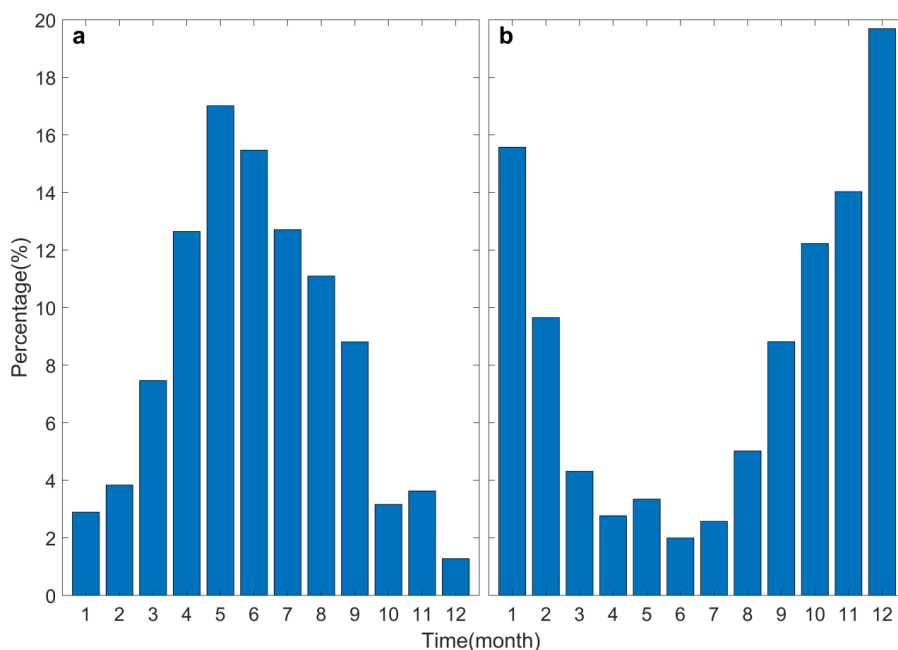
190

191 Figure 4. (a) Time series of the intensity index of the counter-rotating eddy pair in the LS. The red
192 dotted line above (below) represents the sum (difference) of one time the standard deviation and
193 the average value of the time series. Composition of the SSHA for (b) the positive intensity index
194 days and (c) the negative intensity index days. The interval of the SSHA is 0.02 m. This figure is
195 based on HYCOM data.

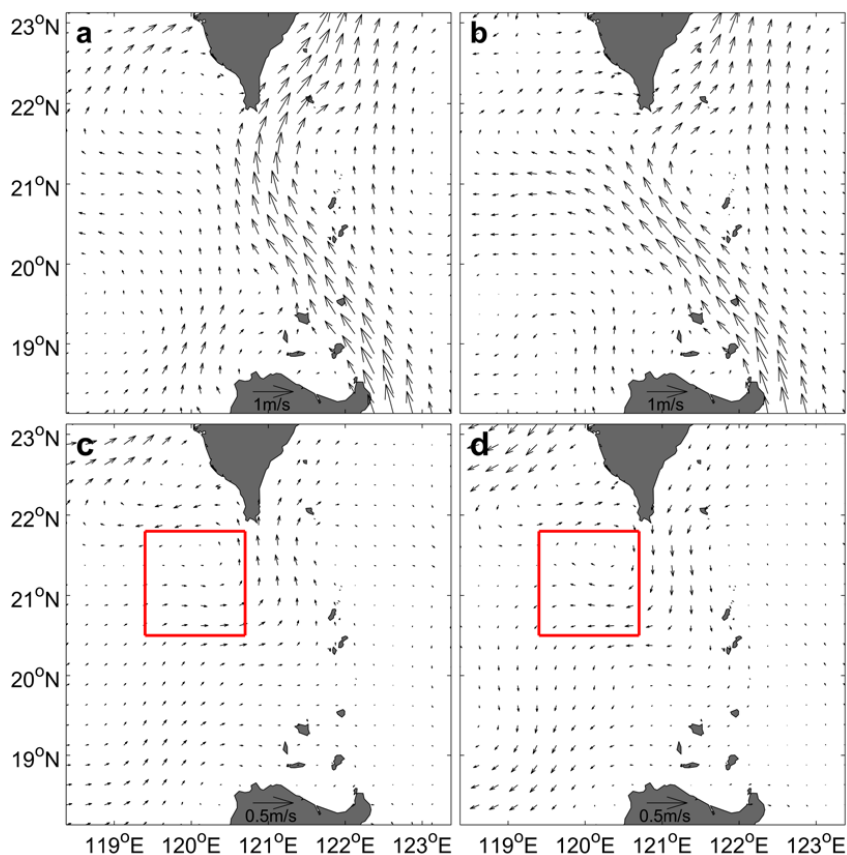
196 We counted the temporal distribution of the positive and negative intensity index values.
197 Figure 5a (Figure 5b) shows that most of the AE (CE) mode of the instances of the
198 counter-rotating eddy pair occurred in the summer (winter) half of the year. The first two months
199 with the highest incidences of the AE (CE) mode occur were May and June (December and
200 January), and their occurrence rates were 17.01% and 15.47% (19.69% and 15.57%), respectively.
201 We constructed the geostrophic current in May and June (Figure 6a) and in December and January



202 (Figure 6b). The patterns of the Kuroshio in Figures 6a and 6b exhibit as the “Leap” and “Loop”
203 patterns of the Kuroshio in the LS, which illustrates that the Leap and Loop patterns of the
204 Kuroshio contribute to the occurrence of the AE mode and the CE mode of the counter-rotating
205 eddy pair, respectively. Figure 6c (Figure 6d) shows that the geostrophic current anomaly in the
206 northern LS is northward (southward). It produces produce positive (negative) vorticity through
207 horizontal velocity shear on the west side of the LS, and then contributes to the formation of a CE
208 (an AE) on the west side of the LS. We will discuss the dynamic mechanism of the
209 counter-rotating eddy pair phenomenon in detail in Section 3.3.



210
211 Figure 5. Seasonal distribution of the occurrence rate for (a) the positive intensity index and (b)
212 the negative intensity index.



213

214 Figure 6. Climatic distribution of geostrophic current in (a) May and June; and (b) December and
215 January; Climatic distribution of the geostrophic current anomaly in (c) May and June; and (d)
216 December and January. The red boxes in the (c) and (d) outline 20.5-21.8°N, 119.4-120.7°E,
217 which represents the position of the mesoscale eddies on the west side of the LS. The figure is
218 based on CMEMS data.

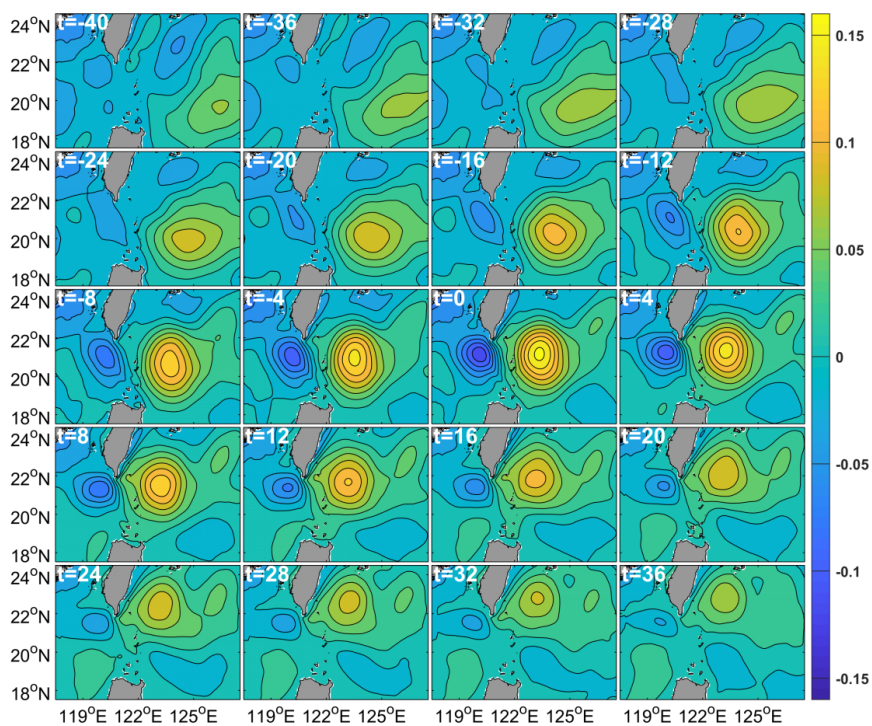
219 3.2 Evolution of the counter-rotating eddy pair in the LS

220 Figure 7 shows the spatial evolution of the AE mode of the counter-rotating eddy pair in the
221 LS. It shows that at the beginning, for example, at $t = -24$, there was a weak AE far away from the
222 east side of LS, but there was no CE on the west of the LS. From $t = -20$ to $t = 0$, as the AE in the



223 NWP approached the northern LS, a CE gradually formed on the west of the LS. At $t = 0$, the AE
224 mode reached the pinnacle. Then from $t = 4$ to $t = 36$, as the AE in the NWP gradually moved
225 away from to the northern LS, the CE on the west of the LS gradually weakened until it finally
226 died out.

227 The growth and weakening of a mesoscale eddy must be accompanied by a change in its
228 relative vorticity. Figure 8a shows that as the AE on the east side of the LS approached and then
229 moved away from the northern LS, its relative vorticity initially decreased first and increased,
230 while the relative vorticity of the corresponding CE on the west side of the LS initially increased
231 and then decreased. The maximum negative (positive) value of the time series of the AE (CE) on
232 the east (west) side of the LS can reached -4.2 s^{-1} (3.6 s^{-1}). These time series had a good
233 correspondence, and their correlation coefficient was -0.97 at the 95% confidence level. Therefore,
234 the temporal variations in the relative vorticity in Figure 8a verify the evolution of the AE mode of
235 the counter-rotating eddy pair in the LS.



236

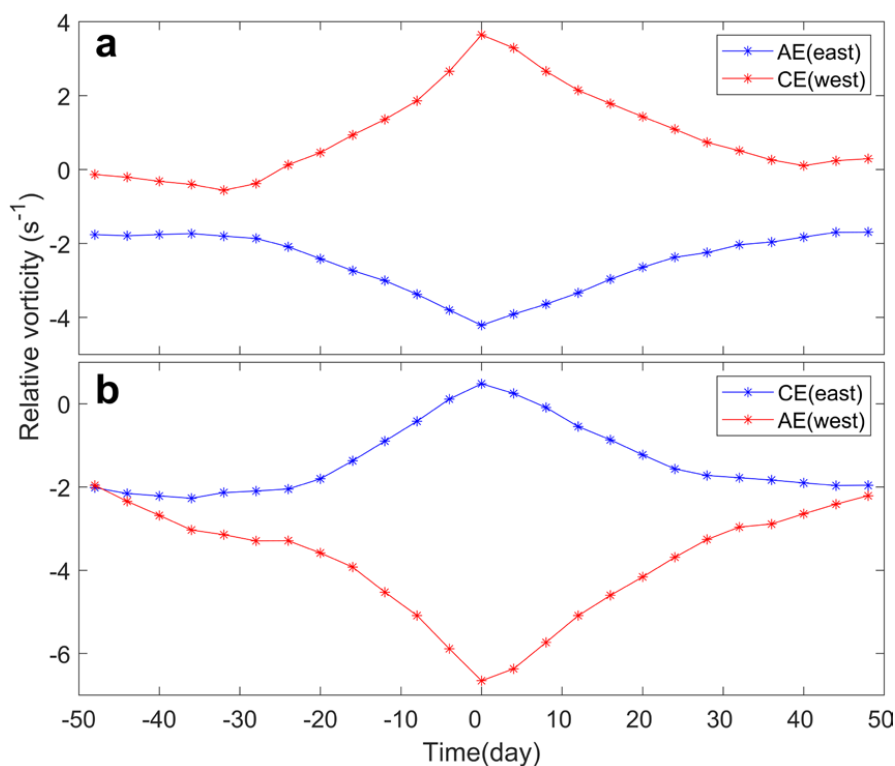
237 Figure 7. Evolution of the AE mode of the counter-rotating eddy pair in the LS based on HYCOM

238 data. The contours and shading both represent the SSHA (unit: m). The interval of the SSHA is

239 0.02 m. The t in the top-left corner of each panel denotes the days before (negative value) or after

240 (positive value) the AE mode of the counter-rotating eddy pair reached the pinnacle ($t=0$). $t = 0$

241 corresponds to the time of the Figure 4b.



242

243 Figure 8. The distribution of the relative vorticity surrounded by the red boxes in Figure 3. (a)

244 Relative vorticity of the AE mode over time. The blue (red) line represents the time series of the

245 relative vorticity of the AE (CE) on the east (west) side of the LS, which corresponds to Figure 7;

246 (b) Relative vorticity of the CE mode over time. The blue (red) line represents the time series of

247 the relative vorticity of the CE (AE) on the east (west) side of the LS, which corresponds to Figure

248 9. This figure is based on HYCOM data.

249 Figure 9 is the same as Figure 7 but for the CE mode of the counter-rotating eddy pair in the

250 LS. It shows that at the beginning, for example, at $t = -32$, there was a weak CE far away from the

251 east side of the LS, but there was no an AE on the west of the LS. From $t = -28$ to $t = 0$, as the CE

252 in NWP approached the northern LS, an AE gradually formed on the west side of the LS. At $t = 0$,

253 the CE mode of the evolution of the counter-rotating eddy pair reached the pinnacle. Then from t

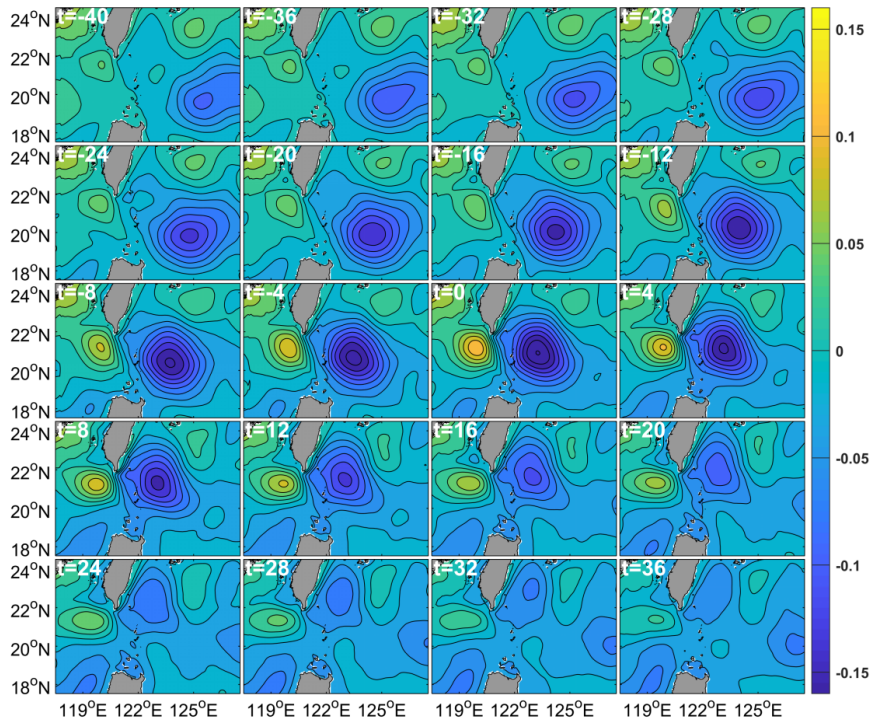


254 = 4 to $t = 36$, as the CE in the NWP gradually moved away from the northern LS, the AE in the
255 west side of the LS gradually weakened until it finally died out. Figure 8b is the same as Figure 8a
256 but for the CE mode. It shows that as the CE on the east side of the LS approached and moved
257 away from the northern LS, its relative vorticity initially increased and then decreased; while the
258 relative vorticity of the corresponding AE on the west side of the LS initially decreased and then
259 increased. The maximum positive (negative) value of the time series of the CE (AE) on the east
260 (west) side of the LS can reach 0.48 s^{-1} (-6.7 s^{-1}). These time series had a good correspondence and
261 their correlation coefficient was -0.96 at the 95% confidence level. Therefore, the temporal
262 variations in the relative vorticity in Figure 8b verify the evolution of the AE mode of the
263 counter-rotating eddy pair in the LS. The evolution of the AE (CE) mode of the counter-rotating
264 eddy pair in the LS is also reflected by the satellite observations (Figures 10 and 11).

265

266

267

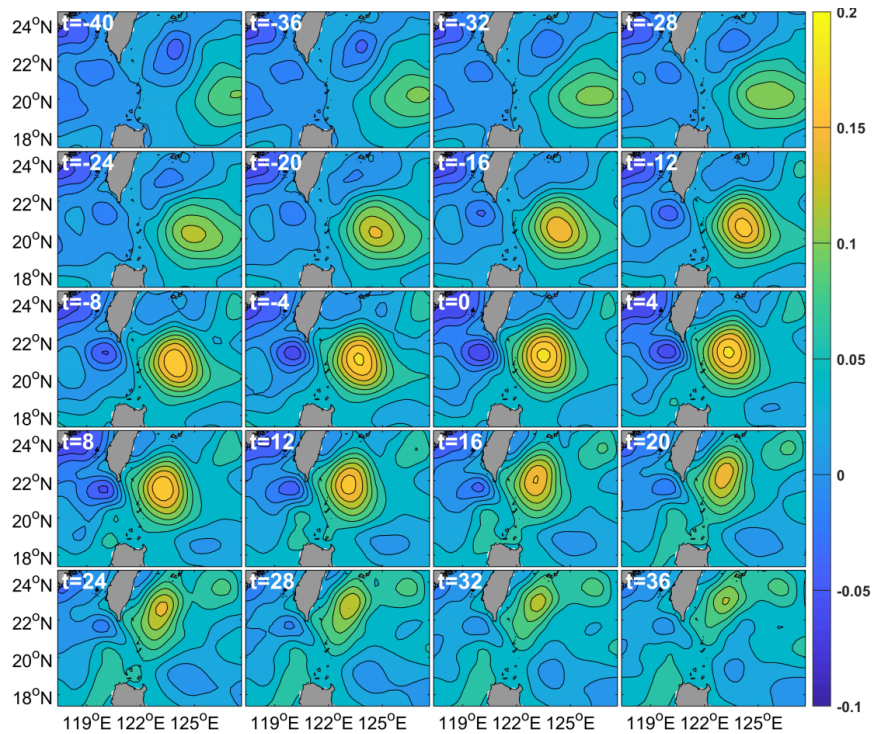


268

269 Figure 9 is the same as Figure 7 but for the CE mode of the counter-rotating eddy pair in the LS.

270

271



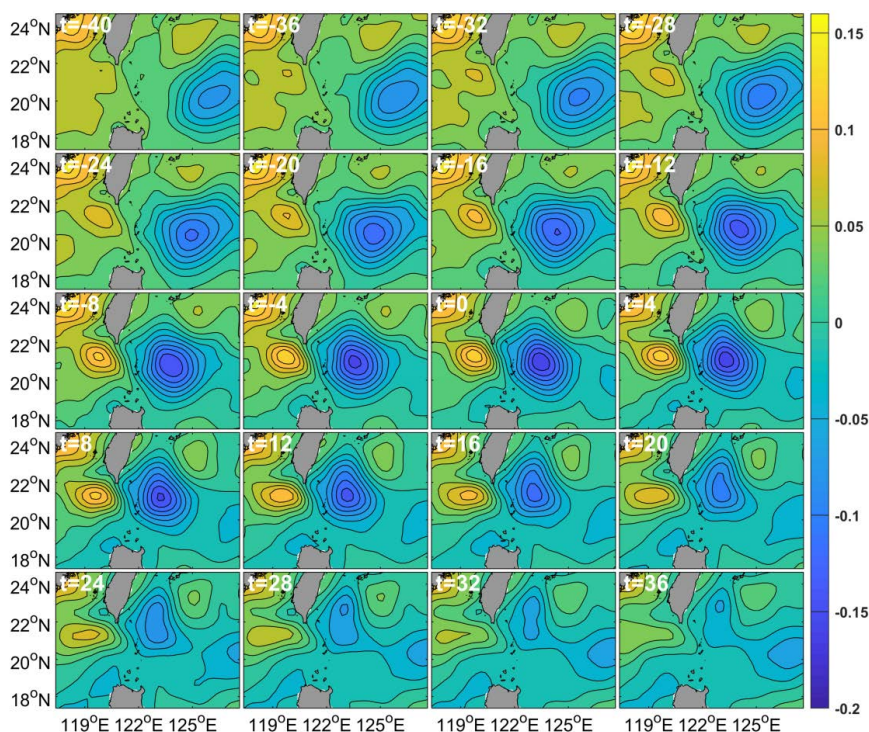
272

273 Figure 10 is the same as Figure 7, but it is based on the CMEMS data.

274

275

276



277

278

Figure 11 is the same as Figure 9, but it is based on the CMEMS data.

279

3.3 Formation mechanism of the counter-rotating eddy pair in the LS

280

Zhang et al. (2017) reported that CEs form mainly due to the barotropic instability caused by

281

horizontal velocity shear of the Kuroshio Loop current southwest of the Taiwan Island. Huang et

282

al. (2019) discovered that an AE from the NWP caused a CE to form on the west side of the LS

283

via horizontal velocity shear. In addition, Figures 4b and 4c show that the dense contour of the

284

SSHA means that there were strong current anomalies and thus strong horizontal velocity shear at

285

the junction of the AE and CE. Therefore, we investigated the role of horizontal velocity shear in

286

the formation of a counter-rotating eddy in the LS.

287

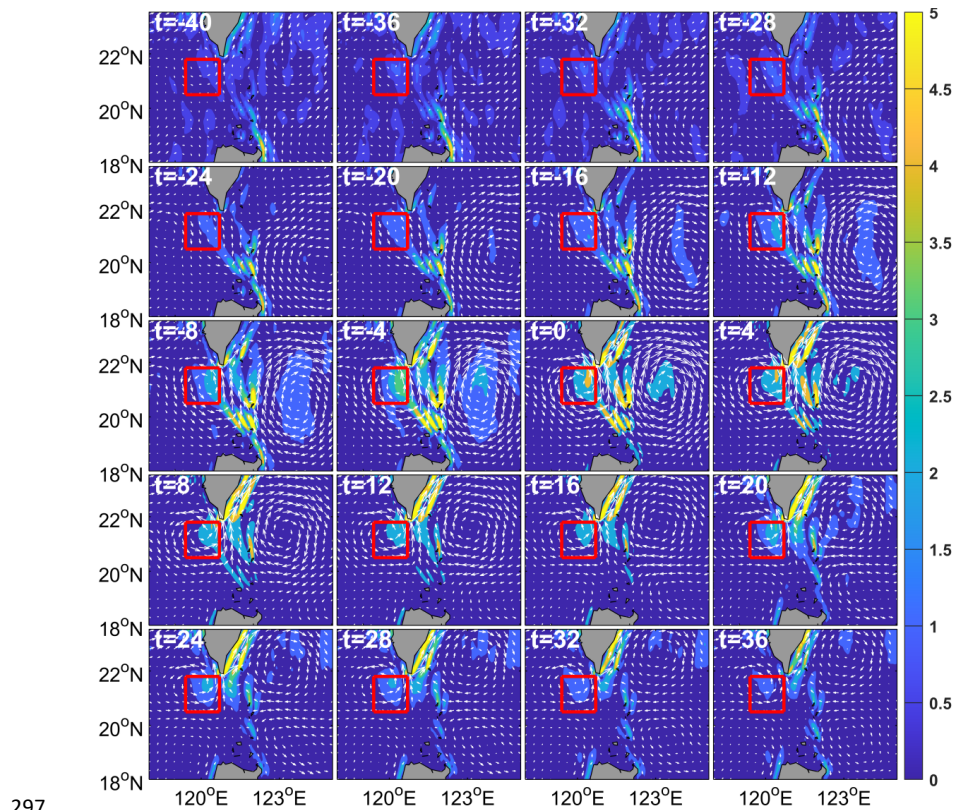
Because meridional horizontal velocity shear is weak, we only show the zonal velocity shear.

288

Figure 12 shows that from $t = -40$ to $t = 0$, as the AE on the east side of the NWP gradually



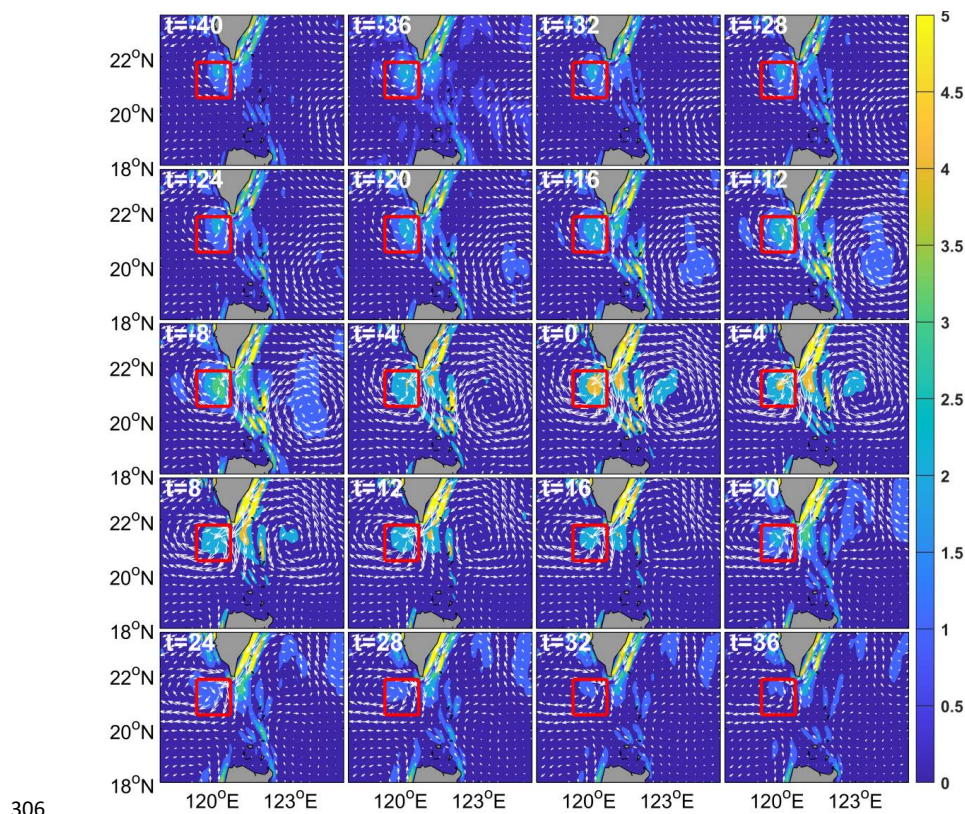
289 approached the northern LS, the absolute value of the zonal horizontal velocity shear ($\frac{\partial v}{\partial x}$)
 290 gradually increased, and a CE gradually formed and strengthened on the west side of the LS. From
 291 $t = 0$ to $t = 36$, as the AE gradually moved away from the northern LS, the absolute value of the
 292 zonal horizontal velocity shear gradually decreased, and the CE on the west side of the LS
 293 gradually weakened. Figure 13 is the same as Figure 12, but for the CE mode of the
 294 counter-rotating eddy pair in the LS. It shows a similar corresponding evolution process. This
 295 demonstrates that there is a good correspondence between the zonal horizontal velocity shear and
 296 the evolution process of the counter-rotating eddy pair.



297
 298 Figure 12 Evolution process of the absolute value of the zonal horizontal velocity shear ($\frac{\partial v}{\partial x}$) for
 299 the AE mode of the counter-rotating eddy pair in the LS based on HYCOM data. The shading



300 represents the zonal horizontal velocity shear (unit: 10^6 s^{-2}). The vector represents the current
301 anomaly. The t in the top-left corner of each panel denotes the days before (negative value) or
302 after (positive value) the AE mode of the counter-rotating eddy pair reached the pinnacle ($t = 0$).
303 Time $t = 0$ corresponds to the time of the Figure 4b. The red boxes on the west side of the LS
304 cover $20.5\text{-}21.8^\circ\text{N}$, $119.4\text{-}120.7^\circ\text{E}$ and represents the location of the CE on the west side of the
305 LS.



306
307 Figure 13 is the same as Figure 12 but for the CE mode of the counter-rotating eddy pair in the
308 LS.

309 However, Figure 12 (Figure 13) shows that zonal horizontal velocity shear only occurred on the
310 right side of the red box, that is, on the right side of the CE (AE). How does the horizontal

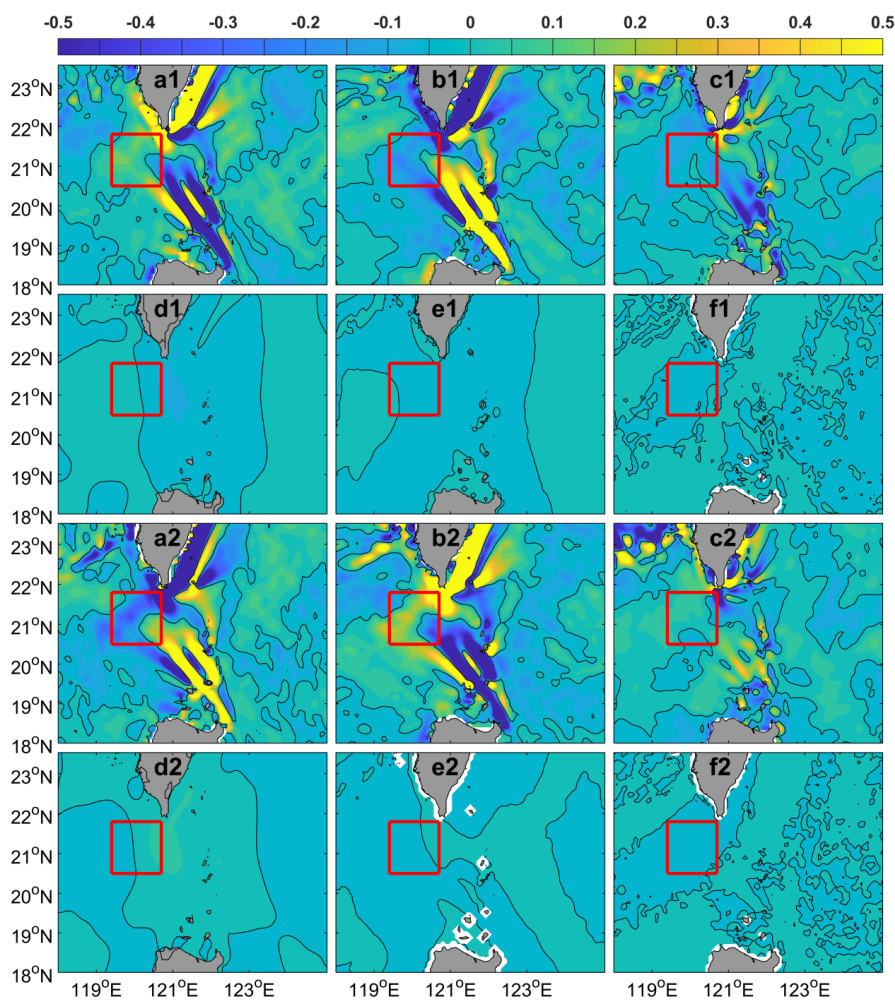


311 velocity shear pass to the entire CE (AE)? To answer this question, we used the vorticity budget
312 equation. Figures 14 (a1 - f1) are for the AE mode of the counter-rotating eddy pair and show the
313 contributions of the zonal advection term, meridional advection term, stretching term, beta term,
314 baroclinic term and diffusion term of the vorticity budget equation, respectively. Compared to the
315 stretching term, the beta term, baroclinic term and diffusion term, the values of the zonal
316 advection term and the meridional advection term in the red box is large. However, most of the
317 values of the meridional advection term in the red box are negative. Only positive vorticity
318 advection can lead to CE formation, which suggests that the zonal advection term is the main
319 cause of the CE formation in the red box. To further test this conclusion, Figure 15a shows the
320 correspondence between the relative vorticity anomaly and the zonal advection of the vorticity in
321 the red box in Figure 14. It shows that there is a good correspondence and their correlation
322 coefficient is as high as 0.96 at the 95% confidence level. Therefore, we conclude that the zonal
323 advection term plays the most important role in the vorticity transport and contributes to the
324 formation of the CE on the west side of LS.

325 Figures 14 (a2 - f2) are the same as Figures 14 (a1 - f1), but for the CE mode of the
326 counter-rotating eddy pair. Figures 14 (a2 - f2) also show that, compared to the stretching term,
327 beta term, baroclinic term, and diffusion term, the values of the zonal advection term and the
328 meridional advection term in the red box are large. However, most of the values of the meridional
329 advection term in the red box are positive. Only negative vorticity advection can lead to AE
330 formation, which implies that the zonal advection term is the main cause of the AE formation in
331 the red box. To further test this conclusion, Figure 15b shows the correspondence between the
332 relative vorticity anomaly and the zonal advection of vorticity. It shows that there is a good



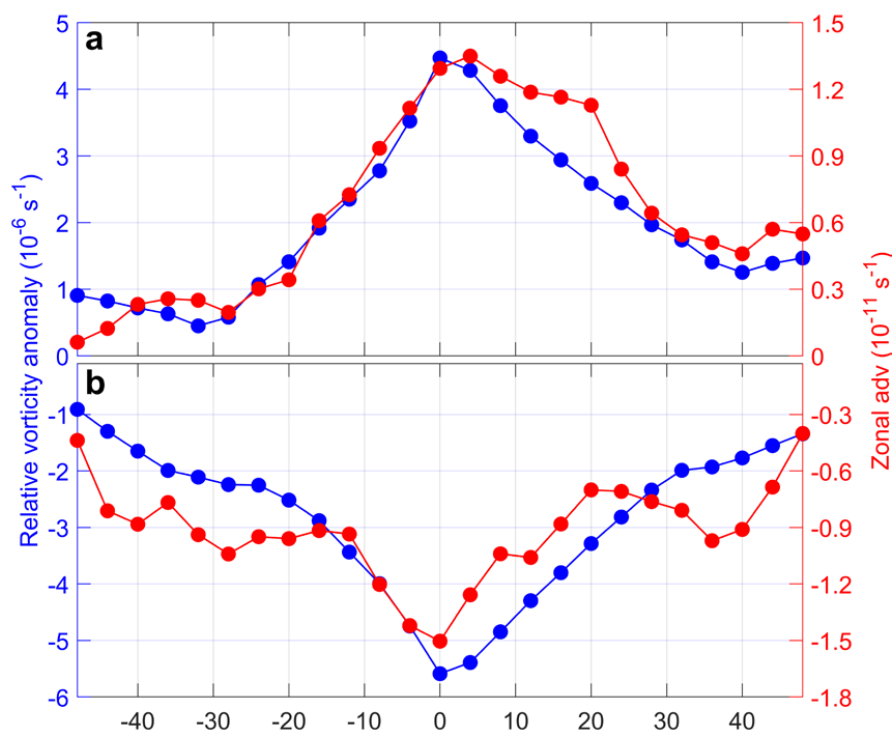
333 correspondence and their correlation coefficient is as high as 0.84 at the 95% confidence level.
334 Therefore, we conclude that the zonal advection term plays the most important role in the vorticity
335 transport and contributes to the formation of the AE on the west side of the LS.



336
337 Figure 14. Vorticity budget equation for (a1 - f1) the AE mode of counter-rotating eddy pair and
338 (a2 - f2) the CE mode of the counter-rotating eddy pair. a1 and a2 represent the zonal advection
339 term; b1 and b2 represent the meridional advection term; c1 and c2 represent the stretching term;
340 d1 and d2 represent the beta term; e1 and e2 represent the baroclinic term; and f1 and f2 represent



341 the diffusion term. The unit is 10^{10} s^{-2} . The red boxes on the west side of the LS border
342 $20.5\text{-}21.8^\circ\text{N}$, $119.4\text{-}120.7^\circ\text{E}$, and they represent the location of the CE or AE on the west side of
343 the LS. The black solid line represents the zero contour. This figure is based on the HYCOM data.



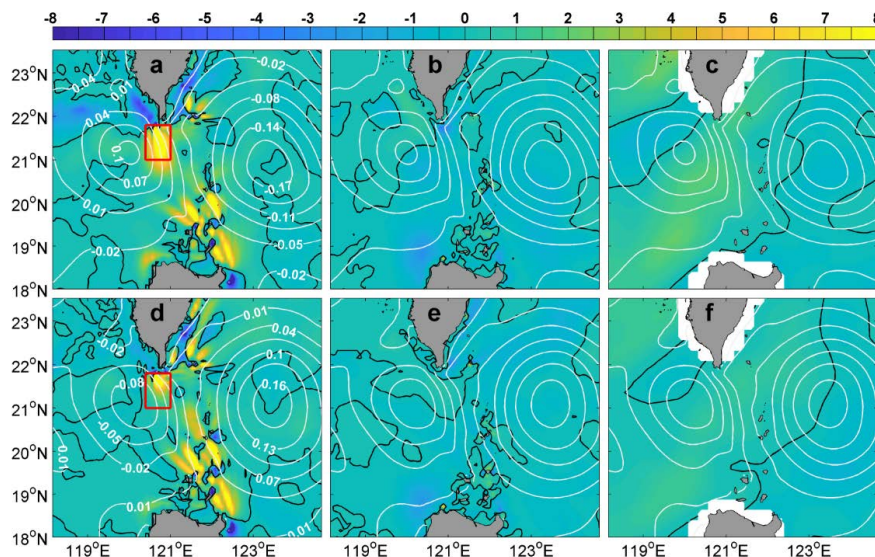
344
345 Figure 15. The distribution of the relative vorticity anomaly and the zonal advection of vorticity
346 surrounded by the red boxes in Figure14 for (a) is for the AE mode of the counter-rotating eddy
347 pair in the LS; and (b) is for the CE mode of the counter-rotating eddy pair in the LS.

348 Above, we have proposed that the horizontal velocity shear caused by the mesoscale eddy on
349 the east side of the LS is transported westward through zonal advection, resulting in the formation
350 of a counter-rotating mesoscale eddy on the west side of the LS. Horizontal velocity shear will
351 inevitably lead to barotropic instability. Now, we will verify our conclusion from the perspective
352 of energy. Figures 16a, 16b, and 16c show that compared to the BC and WW values, the BT



353 values in the LS are large and most of the values are positive, especially in the area surrounded by
354 the red box in Figure 16a, which is the junction of the AE and CE. This means that the BT plays
355 the most important role in the formation of the AE on the west side of the LS.

356 Figures 16d, 16e and 16f show the BT, BC and WW corresponding to the AE mode of the
357 counter-rotating eddy pair in the LS, respectively. Its description and dynamic mechanism are
358 similar to the CE mode of the counter-rotating eddy pair in the LS, so we will discuss the details in
359 this paper.



360
361 Figure 16. (a) BT based on HYCOM data ($10^{-5} \text{ m}^3 \text{ s}^{-3}$) represented by the colors; (b) BC based on
362 HYCOM data ($\text{m}^3 \text{ s}^{-3}$) represented by the colors; (c) WW based on CMEMS surface velocity data
363 and NCDG wind data ($\text{m}^3 \text{ s}^{-3}$) represented by the colors; The red box borders 21°N - 21.8°N ,
364 120.4°E - 121°E . The white contours represent the contours of the SSHA. a, b, and c are for the CE
365 mode of the counter-rotating eddy pair in the LS. d, e and f are for the AE mode of the
366 counter-rotating eddy pair in the LS.

367 **4 Discussion and conclusions**



368 In this study, based on satellite observation data and HYCOM reanalysis data, the
369 counter-rotating eddy pair in the LS was investigated. The phenomenon of counter-rotating eddy
370 pair was defined as the stage when an AE (a CE) in the NWP gradually approached the northern
371 LS, and a CE (an AE) formed on the west side of the LS. This phenomenon exhibited obvious
372 seasonal variation, that is, the AE mode mainly occurred in the summer half of the year, while the
373 CE mode mainly occurred in the winter half of the year. The mean durations of the AE mode and
374 CE mode were both about 70 days. The Leap and Loop patterns of the Kuroshio contributed to the
375 occurrence of the AE mode and CE mode of the counter-rotating eddy pair, respectively. Based on
376 energy analysis and the vorticity budget equation, the dynamic mechanism of the occurrence of a
377 counter-rotating eddy pair is as follows. The AE (CE) in the NWP causes a positive (negative)
378 vorticity anomaly through horizontal velocity shear on the west side of the LS, and the positive
379 (negative) vorticity anomaly is transported westward by the zonal advection of the vorticity,
380 finally leading to the formation of a CE (AE) on the west side of the LS. This conclusion is also
381 verified by barotropic instability based on the energy analysis.

382 However, the research presented in this paper is preliminary and some problems require
383 further study. The occurrence probability of a counter-rotating eddy pair in the LS needs to be
384 determined. The counter-rotating eddy pair phenomenon involves temporal-spatial variations in
385 two mesoscale eddies on both sides of the LS, and it is difficult to provide a quantifiable definition
386 of this phenomenon for a single event. For example, how far apart do the mesoscale eddies on the
387 east and west sides of the LS need to be in order to define them as a counter-rotating eddy pair. We
388 preliminarily calculated that the incidence of this phenomenon was about 5%.

389 Another problem involves threshold of the NWP mesoscale eddies entering the SCS, and



390 what role does the Kuroshio plays in the counter-rotating eddy pair phenomenon in the LS. When
391 we illustrated the counter-rotating eddy pair phenomenon in this study, we eliminated the mean
392 current field, which means that the influence of the Kuroshio was eliminated. However, the role of
393 the Kuroshio in the energy transfer is still worthy of further study. Numerical simulations can be
394 useful to address this issue. Our study provides a new perspective on the energy exchange between
395 the SCS and the NWP.

396

397 **Acknowledges**

398 The authors would like to acknowledge several data sets used in this paper. Satellite remote
399 sensing geostrophic current data and sea level anomaly were obtained from the CMEMS
400 (https://resources.marine.copernicus.eu/?option=com_csw&view=details&product_id=SEALEVE
401 [L_GLO_PHY_L4_REP_OBSERVATIONS_008_047](https://resources.marine.copernicus.eu/?option=com_csw&view=details&product_id=SEALEVE)), the HYCOM reanalysis data were
402 downloaded from HYCOM organization (<https://www.hycom.org/dataserver/gofs-3pt0/>
403 reanalysis), the data set of wind was provided by National Climate Data Center (<https://www.ncdc.noaa.gov/data-access/marineocean-data/blended-global/blended-sea-winds>). Sea surface
404 temperature data comes from Remote Sensing System (<http://www.remss.com/measurements/sea-surface-temperature/>). This study was supported by National Natural Science Foundation of
405 China (grant number 41806019), National Key R&D Program of China (2019YFD0901305), Key
406 R&D projection of Zhejiang Province (2020C03012), National Natural
407 Science Foundation of China (No.41776012), State Key Laboratory of Tropical Oceanography
408 (South China Sea Institute of Oceanology Chinese Academy of Sciences) open topics (grant
409 number LTO2011), Key R&D project of Guangdong
410 number LTO2011), Key R&D project of Guangdong
411 number LTO2011), Key R&D project of Guangdong



412 Province(2020B1111030002), Major science and technology project of Sanya YZBSTC (SKJC-KJ
413 -2019KY03). We thank LetPub (www.letpub.com) for its linguistic assistance during the
414 preparation of this manuscript.

415

416 **Reference**

417 Chang M H, Tang T Y, Ho C R, et al. Kuroshio-induced wake in the lee of Green Island off
418 Taiwan[J]. *Journal of Geophysical Research: Oceans*, 2013, 118(3):1508-1519.

419 Jia Y, Chassignet E P. Seasonal variation of eddy shedding from the Kuroshio intrusion in the
420 Luzon Strait[J]. *Journal of Oceanography*, 2011, 67(5):601-611.

421 Ivchenko V O, Treguier A M, and Best S E. A kinetic energy budget and internal instabilities in the
422 fine resolution antarctic model, *Journal of Physical Oceanography*, 1997, 27:5-22.

423 Lien R C, Ma B, Cheng Y H, et al. Modulation of Kuroshio transport by mesoscale eddies at the
424 Luzon Strait entrance[J]. *Journal of Geophysical Research: Oceans*, 2014, 119(4):2129-2142.

425 Lu J, Liu Q. Gap-leaping Kuroshio and blocking westward-propagating Rossby wave and eddy in
426 the Luzon Strait[J]. *Journal of Geophysical Research Oceans*, 2013, 118(3):1170-1181.

427 Oey L Y. Loop Current and Deep Eddies[J]. *Journal of Physical Oceanography*, 2008, 38(7): 1426
428 -1449.

429 Pedlosky J. *Geophysical Fluid Dynamics*, 1987, 2nd ed., 710 pp., Springer, N. Y.

430 Pujol M I, Françoise M. Product user manual for sea level SLA products, 2019.06 (<http://marine.copernicus.eu/>).

432 Sun R, Ling Z, Chen C, Yan Y. Interannual variability of thermal front west of Luzon Island in
433 boreal winter[J]. *Acta Oceanologica Sinica*, 2015, (34):108.

434 Sun R, Wang G, Chen C. The Kuroshio bifurcation associated with islands at the Luzon Strait[J].



- 435 Geophysical Research Letters, 2016a, 43(11):5768-5774.
- 436 Sun R, Gu Y, Li P, et al. Statistical characteristics and formation mechanism of the Lanyu cold
437 eddy[J]. Journal of Oceanography, 2016b, 72(4):641-649.
- 438 Sun R, Zhai F, Gu Y. The Four Patterns of the East Branch of the Kuroshio Bifurcation in the
439 Luzon Strait[J]. Water, 2018, 10(12).
- 440 Sheu W J, Wu C R, Oey L Y. Blocking and Westward Passage of Eddies in the Luzon Strait[J].
441 Deep Sea Research Part II: Topical Studies in Oceanography, 2010, 57(19-20):0-1791.
- 442 Wang Q, Zeng L, Chen J, et al. The linkage of Kuroshio intrusion and mesoscale eddy variability
443 in the northern South China Sea: subsurface speed maximum. Geophysical Research Letters,
444 2020, 47(11).
- 445 Yan X, Zhu X H, Pang C, et al. Effects of mesoscale eddies on the volume transport and branch
446 pattern of the Kuroshio east of Taiwan[J]. Journal of Geophysical Research: Oceans, 2016,
447 121(10): 7683-7700.
- 448 Yang H, Wu L, Liu H, et al. Eddy energy sources and sinks in the South China Sea[J]. Journal of
449 Geophysical Research Oceans, 2013, 118(9):4716-4726.
- 450 Zhang Z, Wang W, Qiu B. Oceanic mass transport by mesoscale eddies[J]. Science, 2014,
451 345(6194):322-324.
- 452 Zhang Z, Zhao W, Tian J, et al. A mesoscale eddy pair southwest of Taiwan and its influence on
453 deep circulation[J]. Journal of Geophysical Research Oceans, 2013, 118(12):6479-6494.
- 454 Zhang Z, Zhao W, Tian J, et al. Spatial structure and temporal variability of the zonal flow in the
455 Luzon Strait[J]. Journal of Geophysical Research Oceans, 2015, 120(2).
- 456 Zhang Z, Zhao W, Qiu B, et al. Anticyclonic Eddy Sheddings from Kuroshio Loop and the



- 457 Accompanying Cyclonic Eddy in the Northeastern South China Sea[J]. Journal of Physical
458 Oceanography, 2017, 47(6):1243-1259.
- 459 Zhang H M, Reynolds R W, Bates J J, et al. Blended and gridded high resolution global sea
460 surface wind speed and climatology from multiple satellites: 1987-present. American
461 Meteorological Society 2006 Annual Meeting, Vol. 2.
- 462 Zheng Q, Tai C K, Hu J, et al. Satellite altimeter observations of nonlinear Rossby eddy-Kuroshio
463 interaction at the Luzon Strait[J]. Journal of oceanography, 2011, 67(4): 365-376.